

# Deep Domain Adversarial Adaptation for Photon-efficient Imaging

Yiwei Chen, Gongxin Yao, Yong Liu, Hongye Su, and Yu Pan\*

*State Key Laboratory of Industrial Control Technology, Hangzhou, 310027, P. R. China and  
College of Control Science and Engineering, Zhejiang University, Hangzhou, 310027, P. R. China*

Xiaomin Hu

*CAS Key Laboratory of Quantum Information, University of Science and Technology of China, Hefei, 230026, P. R. China and  
CAS Center For Excellence in Quantum Information and Quantum Physics,  
University of Science and Technology of China, Hefei, 230026, P. R. China*

(Dated: May 11, 2022)

Photon-efficient imaging with the single-photon LiDAR captures the 3D structure of a scene by only a few detected signal photons per pixel. However, the existing computational methods for photon-efficient imaging are pre-tuned on a restricted scenario or trained on simulated datasets. When applied to realistic scenarios whose signal-to-background ratios (SBR) and other hardware-specific properties differ from those of the original task, the model performance often significantly deteriorates. In this Letter, we present a domain adversarial adaptation design to alleviate this domain shift problem by exploiting unlabeled real-world data, with significant resource savings. This method demonstrates superior performance on simulated and real-world experiments using our home-built up-conversion single-photon imaging system, which provides an efficient approach to bypass the lack of ground-truth depth information in implementing computational imaging algorithms for realistic applications.

Single-photon light detection and ranging (LiDAR) systems have achieved dramatic success in 3D imaging over the past decades [1–5]. Benefiting from the high sensitivity of single-photon avalanche diode (SPAD) detector [6, 7], single-photon LiDAR provides better precision over a longer distance as compared to the traditional systems based on the photomultiplier tube [8]. In practice, a photon counting histogram is collected at each scanned point with the time-correlated single photon counting (TCSPC) technique [9], which records the timestamps of emitted and reflected photons for the time-of-flight (ToF) calculation. However, due to practical constraints on optical flux and integration time, the average number of detected photons per pixel, including signal and noise counts, could be less than a few dozens. This calls for photon-efficient imaging [10, 11], whose goal is to recover a precise depth image from a sparsely distributed histogram of few photon counts.

Machine learning methods, including statistical [11, 12] and deep learning models [13–15], have been proposed for photon-efficient imaging. Particularly, deep learning models have demonstrated remarkable performance in terms of reconstruction accuracy and inference time. Deep learning model needs huge amounts of data for training, whereas it is extremely difficult to acquire enough annotated real-world data. As a result, the existing models are trained on simulated datasets for which the signal-to-background ratio (SBR) and other hardware-specific properties have to be assumed. For example, SBR could be affected by light condition, object distance or noise inherent in the hardware, such as the dark counts of SPAD and pump light [16]. Hardware-

specific properties also include the shape of a pulse [17]. Therefore, the model trained on simulated dataset may not generalize well to realistic hardware or environment for which SBR or pulse shape are different, causing the domain shift problem [18–20]. Although a calibration step can be conducted to estimate the realistic parameters, regenerating enough simulated data and retraining the model to fit the target domain requires tens of hours and a huge amount of computational resources, which is highly expensive and unscalable. Considering that ground-truth label is basically inaccessible in a real-world experiment, training the deep learning model with real-world data is even more impossible.

In this paper, we propose a deep domain adversarial adaptation method with a novel network structure to tackle this domain shift problem. This method only requires dozens of extra training iterations with a small amount of unlabeled data from the target domain for the model to adapt to different SBR or hardware-specific properties. Extensive experiments on the simulated datasets demonstrate the efficiency of our method for the model to adapt to different SBRs. Moreover, the real-world experiment based on our home-built single-photon imaging system shows that our method improves the baseline model performance by a remarkable margin, while other statistical and deep learning algorithms do not generalize well to the realistic scenario.

The domain adversarial adaptation method is adopted mainly from [21] and its schematic diagram is shown in Fig. 1. The feature extractor, denoted by  $\mathcal{F}$ , learns the transformation that maps both domains into a common feature space. The purpose of this transformation is to extract domain-independent features from the inputs to confuse the discriminator, while the discriminator, denoted by  $\mathcal{D}$ , tries to determine whether these features

\* ypan@zju.edu.cn

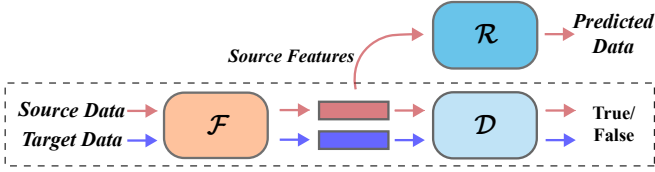


FIG. 1. Schematic diagram of the deep domain adversarial adaptation scheme.  $\mathcal{F}$ , feature extractor;  $\mathcal{D}$ , discriminator;  $\mathcal{R}$ , reconstructor. We use red and blue colors to indicate the pipelines on the source and target domain, respectively.

are from the source or the target domain. This process, as marked by the dashed box, corresponds to a minimax two-player game which forces  $\mathcal{F}$  to focus on capturing the similarity of the two domains. Meanwhile, the reconstructor denoted by  $\mathcal{R}$  learns to estimate the ground-truth depth from the source features.

In principle, this scheme can be applied to any deep learning model as long as a suitable feature space has been defined. Nevertheless, existing deep learning models either involve complex attention operations [14] or residual connections [15], which makes it difficult to find an encoder-decoder division for adversarial adaptation training. Therefore, we propose a simple yet efficient encoder-decoder network structure design for the domain adaptation task. Firstly, inspired by [22] and [23], we design a spatiotemporal block (ST-Block) which consists of four branches based on the spatiotemporal convolution.  $\mathcal{F}$  is built by stacking eight modules, each composed of an ST-Block and a 3D pooling layer. Then  $\mathcal{R}$  comprises seven deconvolutional layers and a  $1 \times 1 \times 1$  convolutional layer. In particular, each convolutional and deconvolutional layer is followed by a group normalization layer and a rectified linear unit (ReLU) activation. We name the whole composition of  $\mathcal{F}$  and  $\mathcal{R}$  as the spatiotemporal inception network (STIN). The details of STIN are given in Supplemental Material.

STIN is first trained on the source domain as a baseline model. Here the depth estimation is taken as a classification problem, in which STIN aims at correctly classifying each pixel into a depth category that matches its ground-truth depth [24]. The photon counting histograms  $H \in \mathbb{R}^{N_x \times N_y \times T}$  for the source domain are generated by simulation from the ground-truth depth images  $D \in \mathbb{R}^{N_x \times N_y}$ , where  $T$ ,  $N_x$  and  $N_y$  are the number of time bins, the horizontal and vertical resolutions, respectively. The prediction of the model is denoted as  $\hat{H} \in \mathbb{R}^{N_x \times N_y \times T}$ . Note that  $D$  has to be further processed by the following rounding function for classification,

$$d_{i,j} = [d_{i,j}] = \max\{n \in \mathbb{Z}_0^+ \mid n \leq \frac{2d_{i,j}}{\Delta \cdot c}\}, \quad (1)$$

where  $c$  is the light speed and  $\Delta$  is the size of time bin. The cross-entropy (CE) loss between  $\hat{H}$  and  $D$  is given by

$$\mathcal{L}_{\text{CE}}(\hat{H}, D) = \sum_{i,j} \mathcal{L}_{\text{CE}}(\hat{h}_{i,j}, d_{i,j}^{(o)}) \quad (2)$$

---

### Algorithm 1 Implementation of DANN

---

**Input:**

- 1: samples:  $\mathbf{S} = \{(H_s^{(i)}, D_s^{(i)})\}_{i=1}^N$  and
- 2:  $\mathbf{T} = \{H_t^{(i)}\}_{i=1}^{N'}$ ;
- 3: adaptation weight  $\lambda_a$ ;
- 4: pre-trained  $\mathcal{F}$  and  $\mathcal{R}$  on the source domain;
- 5: randomly initialized  $\mathcal{D}$ ;

**Output:** new  $\mathcal{F}$  and  $\mathcal{R}$ ;

- 6: **while** stopping criterion is not met **do**
  - 7:   **for**  $i \leftarrow 1, \dots, N$  **do**
  - 8:     Randomly sample  $j$  from  $\{1, \dots, N'\}$ ;
  - 9:     Calculate  $\mathcal{L}_{\text{adv}}(H_s^{(i)}, H_t^{(j)})$ ;
  - 10:     Update  $\mathcal{D}$  by minimizing  $\mathcal{L}_{\text{adv}}$ ;
  - 11:     Calculate the total loss by
  - 12:          $\mathcal{L}_{\text{total}}(H_s^{(i)}, D_s^{(i)}, H_t^{(j)}) \leftarrow$
  - 13:              $\mathcal{L}(H_s^{(i)}, D_s^{(i)}) - \lambda_a \cdot \mathcal{L}_{\text{adv}}(H_s^{(i)}, H_t^{(j)})$ ;
  - 14:     Update  $\mathcal{F}$  and  $\mathcal{R}$  by minimizing  $\mathcal{L}_{\text{total}}$ ;
  - 15:   **end for**
  - 16: **end while**
- 

which is adopted from [24], and  $\mathbf{d}_{i,j}^{(o)} \in \mathbb{R}^T$  is the one-hot encoding of  $d_{i,j}$ . Another total variation (TV) regularization term  $\mathcal{L}_{\text{TV}}$  for smoothing the prediction [15] is added to make the total loss function as

$$\mathcal{L} = \mathcal{L}_{\text{CE}} + \lambda_{\text{TV}} \cdot \mathcal{L}_{\text{TV}}, \quad (3)$$

where  $\lambda_{\text{TV}}$  is the weight of the TV term.

The goal of the discriminator is to distinguish between the source and target domain from the latent features. Thus,  $D$  has to maintain the temporal dimension of the features, while the spatial dimension of the features needs to be blurred. To do this, the latent features first go through a 3D pooling layer with a kernel size of  $1 \times 8 \times 8$ . After that, three fully-connected layers will map these features to a scalar that classifies the input into either the source or the target domain.

Domain adversarial training is achieved by alternatively minimizing the following loss functions,

$$\mathcal{L}(H_s, D_s) = \mathcal{L}(\mathcal{R}(\mathcal{F}(H_s)), D_s), \quad (4)$$

$$\mathcal{L}_{\text{adv}}(H_s, H_t) = \log \mathcal{D}(\mathcal{F}(H_s)) - \log(1 - \mathcal{D}(\mathcal{F}(H_t))), \quad (5)$$

where  $H_s$  and  $D_s$  are the sample and ground-truth depth from the source domain, and  $H_t$  is the sample from the target domain. It should be noted that the ground-truth depth of the target domain is not needed for domain adversarial training. In each training iteration,  $\mathcal{D}$  is firstly optimized by minimizing the domain adversarial loss defined in Eq. (5) to extract domain-invariant features. Then  $\mathcal{F}$  and  $\mathcal{R}$  are simultaneously optimized by minimizing the total loss function given by

$$\mathcal{L}_{\text{total}} = \mathcal{L} - \lambda_a \cdot \mathcal{L}_{\text{adv}} \quad (6)$$

to improve the reconstruction performance, with  $\lambda_a$  being the weight of adaptation. The detailed implementation

TABLE I. Comparisons of the baseline and DANN-based model on simulated datasets. Best results are highlighted in bold. The percentage difference from the baseline is also shown in the parentheses. The definitions for the metrics RMSE and Abs rel are given in Supplemental Material.

SBR	Baseline		DANN-based STIN	
	RMSE	Abs rel	RMSE	Abs rel
2:2	<b>0.026</b>	<b>0.018</b>	0.031(↑ 19.6%)	0.019(↑ 3.8%)
2:50	0.121	0.036	<b>0.076(↓ 37.1%)</b>	<b>0.028(↓ 24.9%)</b>
2:100	0.388	0.147	<b>0.088(↓ 77.3%)</b>	<b>0.040(↓ 72.5%)</b>

of domain adversarial neural network (DANN) training is shown in Algorithm 1.

The validation experiments are firstly conducted on the simulated dataset. The goal is to adapt the model pre-trained on low-noise domain to high-noise domain. 15940 low-noise samples with ground-truth depth information and 42 high-noise samples without ground-truth information are generated from NYU v2 dataset [25] as the training set using the observation model described in Supplemental Material. The total number of time bin is 1024 and the bin size is 80 picoseconds (ps). The waveform of the emitted pulsed is assumed to have an ideal Gaussian shape with the full width at half maximum of 400 ps. Constrained by GPU memory size, we divide the training samples into patches of size [1024, 32, 32] and set the batch size to 6. The SBRs for generating the low-noise and high-noise samples are {2:2, 5:2, 10:2} and {2:50, 2:100}, respectively. Here an SBR of  $n:m$  stands for the ratio of the average number of signal photons to noise photons per pixel. The test set is composed of samples with SBRs of {2:2, 2:50, 2:100}, which are generated from Middlebury dataset [26] with a resolution of  $512 \times 512$ . As noted before, the STIN is first trained on the low-noise dataset as the baseline model. The training takes about 10 hours. Then the trained model is adapted to the high-noise domain using the 42 high-noise samples by domain adversarial training, which takes only about 10 minutes. In testing, the high resolution input image is divided into small patches for depth prediction and then the outputs are concatenated into a large image. As shown in Table I, the baseline model does not generalize well to the high-noise test samples with SBR of 2:50 or 2:100, whereas the DANN-based adaptation method achieves a significant improvement at low SBRs. Particularly, the DANN-based model outperforms the baseline by 77.3% in RMSE and 72.5% in Abs rel when SBR is 2:100. At the high SBR of 2:2, the performance of DANN-based model is worse than the baseline model, since the baseline is trained solely with this SBR. Meanwhile, the DANN-based model has to adapt to high-noise samples, which inevitably decreases its performance at SBR=2:2 since the model needs to balance between two domains.

Fig. 2 shows the predicted depth images for the Laundry scene from the test set. We see that the baseline can

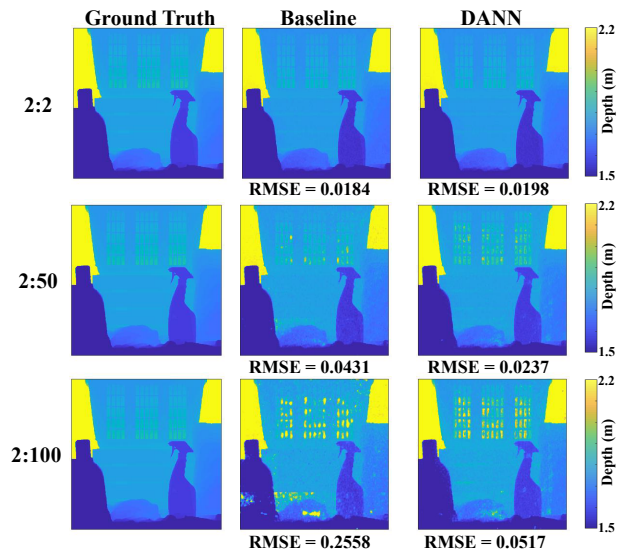


FIG. 2. The predicted depth images of the Laundry scene by STIN and DANN-based STIN.

precisely recover the depth image at high SBRs, whereas many erroneous regions appear when SBR decreases. In contrast, the performance of the DANN-based model is much more robust to the decrease in SBR.

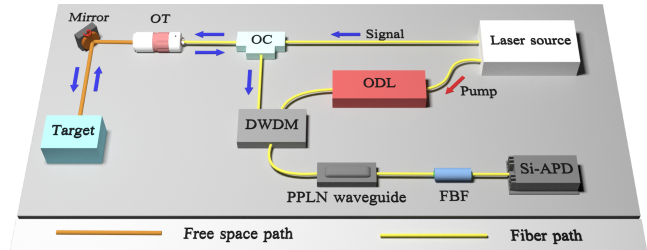


FIG. 3. Schematic diagram of our imaging system. ODL, optical delay line; OC, optical circulator; OT, optical transceiver; DWDM, dense wavelength division multiplexing; PPLN waveguide, periodically poled lithium niobate waveguide; FBF, fiber bandpass filter; Si-APD, silicon avalanche photodiodes.

Next, we conduct real-world experiment by building a single-photon imaging system, whose schematic diagram is shown in Fig. 3. The system is based on an upconversion process that transforms the near-infrared signal photon to the visible regime for detection [16]. The picosecond laser source emits synchronized pump pulses (1565.5nm) and signal pulses (1554.1nm). The signal pulse is sent to the programmable micro-electromechanical system (MEMS) mirror through an optical transceiver for target scan. The signal and pump pulses are combined for the sum frequency generation process in the PPLN waveguide. The time delay of the pump pulse is controlled by the programmable motorized ODL. By adjusting the delay time such that the signal and

pump pulses coincide, the visible light (779.8nm) is generated. The generated photons are then passed through several home-built FBFs to the Si-APD. We use a field-programmable gate array (FPGA) to count the number of detected photons at each time-delay step. A desktop computer is employed to control the MEMS mirror and ODL. Unlike [16], we use commercially packaged PPLN waveguide instead of bulk PPLN crystal in the conversion module. Compared with bulk crystal, the waveguide has higher upconversion efficiency with a more stable all-fiber structure.

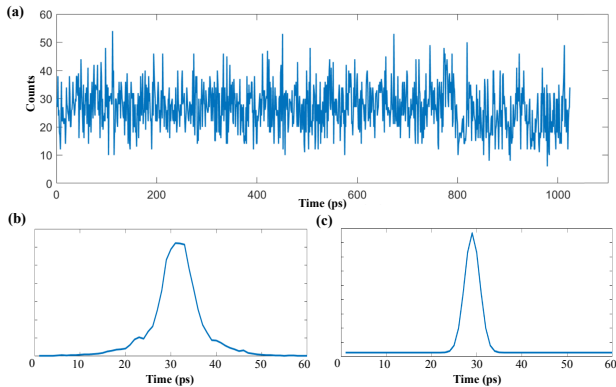


FIG. 4. (a) Noise photon counts of our system. (b) Detected photon counts of our system. (c) The ideal pulse shape used for simulation.

The detected noise photons as shown in Fig. 4 (a) come from the environment, dark counts of the SPAD and the pump light. In particular, the frequency-doubled photons of the pump light that cannot be completely eliminated by the optical filters constitute the major source of noise, whereas the simulation only assumes a uniform distribution for ambient noise. Besides, it can be observed that there is a visible difference between the real-world waveform of detected photons in Fig. 4 (b) and the simulated waveform in Fig. 4 (c). Therefore, the noise source, statistics and detected waveform of our system substantially differ from the ideal simulation, which makes it a perfect candidate for the validation of the domain adaptation method.

The 2022 Asian Games mascot Chenchen is placed outdoors and about 5 meters away from the optical transceiver. The ODL is scanned in 1 ps steps over a range of 1024 ps. In order to simulate photon-efficient imaging, we set the acquisition time for each time delay step as 1 microsecond such that no more than dozens of signal and noise photons are recorded at each pixel. The baseline STIN is pre-trained on the simulated dataset with SBRs of {2:10, 2:50, 2:100}. By adjusting the number of optical filters, the overall SBR of our system is measured to be 0.103, which does not overlap with the SBRs for pre-training. The pre-trained STIN is then tuned by several patches with the resolution of [1024, 32, 32] from the real-world data using the proposed domain adversarial adaptation method. The domain

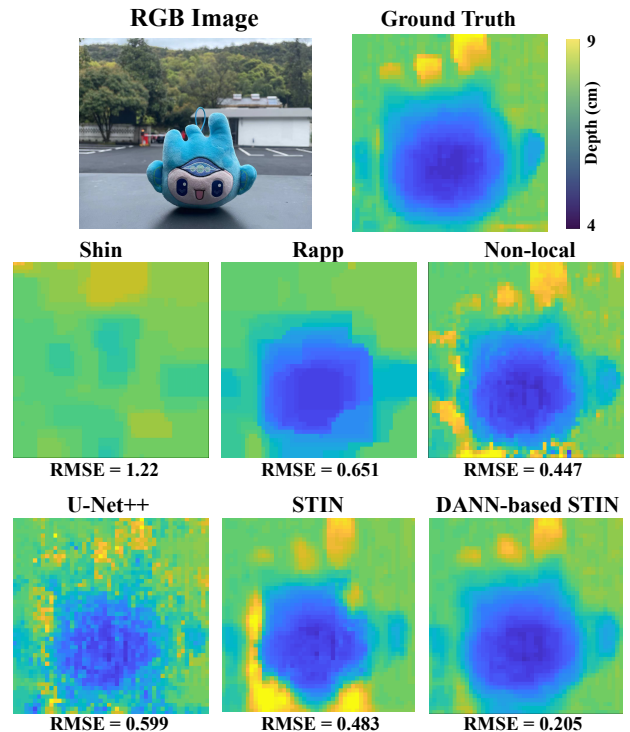


FIG. 5. The reconstruction results of 2022 Asian Games mascot Chenchen with a spatial resolution of  $48 \times 48$ . The approximated ground-truth depth image is obtained by increasing the acquisition time at each time-delay step to one millisecond [14]. The estimated ground-truth data are only used for evaluation but not for adaptation.

adaptation process takes only several minutes, without using any ground-truth depth information in the real world. As shown in Fig. 5, our method achieves a significant visual improvement when compared to other state-of-the-art competitors, including two statistical methods [11, 12], two deep learning models [14, 15] and the baseline model. These competitors all have shown good performance on the simulated dataset as detailed in Supplemental Material and poor generalizability in real experiment, which highlights the necessity of domain adaptation. In particular, the DANN-based STIN achieves the highest imaging quality with a decrease in RMSE of 57.5%, 65.8% and 54.1% as compared to baseline, U-Net++ and Non-local net, respectively.

In conclusion, we propose an efficient domain adversarial adaptation method to improve the depth estimation precision for a 3D scene, without using any ground-truth depth information of the target domain. Experimental results on simulated dataset and our home-built imaging system have verified the effectiveness of our method. It has been shown that although the pre-trained models may be effective on the simulated dataset, their performance may deteriorate significantly if domain adaptation is not conducted. Considering that obtaining sufficient data, either real-world data with ground-truth labels or simulated data, to retrain the model in the target do-

main is extremely time-consuming or merely impossible, the proposed approach of this paper is able to provide significant resource savings for the practical deployment of deep learning models in photon-efficient imaging applications.

## ACKNOWLEDGMENTS

This work was supported by the National Natural Science Foundation of China (Grant No. 62173296) and National Key R&D Program of China (Grant No. 2018YF1700100).

- 
- [1] A. Kirmani, D. Venkatraman, D. Shin, A. Colaço, F. N. Wong, J. H. Shapiro, and V. K. Goyal, First-photon imaging, *Science* **343**, 58 (2014).
- [2] R. Lussana, F. Villa, A. Dalla Mora, D. Contini, A. Tosi, and F. Zappa, Enhanced single-photon time-of-flight 3D ranging, *Opt. Express* **23**, 24962 (2015).
- [3] Y. Altmann, S. McLaughlin, M. J. Padgett, V. K. Goyal, A. O. Hero, and D. Faccio, Quantum-inspired computational imaging, *Science* **361**, eaat2298 (2018).
- [4] G. Musarra, A. Lyons, E. Conca, Y. Altmann, F. Villa, F. Zappa, M. Padgett, and D. Faccio, Non-line-of-sight three-dimensional imaging with a single-pixel camera, *Phys. Rev. Appl.* **12**, 011002 (2019).
- [5] Z.-P. Li, X. Huang, Y. Cao, B. Wang, Y.-H. Li, W. Jin, C. Yu, J. Zhang, Q. Zhang, C.-Z. Peng, *et al.*, Single-photon computational 3D imaging at 45 km, *Photonics Res.* **8**, 1532 (2020).
- [6] R. H. Hadfield, Single-photon detectors for optical quantum information applications, *Nat. Photonics* **3**, 696 (2009).
- [7] K. L. Nicolich, C. Cahall, N. T. Islam, G. P. Lafyatis, J. Kim, A. J. Miller, and D. J. Gauthier, Universal model for the turn-on dynamics of superconducting nanowire single-photon detectors, *Phys. Rev. Appl.* **12**, 034020 (2019).
- [8] B. Dolgoshein, V. Balagura, P. Buzhan, M. Danilov, L. Filatov, E. Garutti, M. Groll, A. Ilyin, V. Kantserov, V. Kaplin, *et al.*, Status report on silicon photomultiplier development and its applications, *Nucl. Instrum. Methods Phys. Res. A* **563**, 368 (2006).
- [9] D. O'Connor, *Time-correlated single photon counting* (Academic press, 2012).
- [10] D. Shin, A. Kirmani, V. K. Goyal, and J. H. Shapiro, Photon-efficient computational 3-D and reflectivity imaging with single-photon detectors, *IEEE Trans. Comput. Imaging* **1**, 112 (2015).
- [11] D. Shin, F. Xu, D. Venkatraman, R. Lussana, F. Villa, F. Zappa, V. K. Goyal, F. N. Wong, and J. H. Shapiro, Photon-efficient imaging with a single-photon camera, *Nat. Commun.* **7**, 1 (2016).
- [12] J. Rapp and V. K. Goyal, A few photons among many: Unmixing signal and noise for photon-efficient active imaging, *IEEE Trans. Comput. Imaging* **3**, 445 (2017).
- [13] D. B. Lindell, M. O'Toole, and G. Wetzstein, Single-photon 3D imaging with deep sensor fusion, *ACM Trans. Graph.* **37**, 113 (2018).
- [14] J. Peng, Z. Xiong, X. Huang, Z.-P. Li, D. Liu, and F. Xu, in *European Conference on Computer Vision (ECCV)* (2020) pp. 225–241.
- [15] Z. Zang, D. Xiao, and D. D.-U. Li, Non-fusion time-resolved depth image reconstruction using a highly efficient neural network architecture, *Opt. Express* **29**, 19278 (2021).
- [16] P. Rehai, Y. M. Sua, S. Zhu, I. Dickson, B. Muthuswamy, J. Ramanathan, A. Shahverdi, and Y.-P. Huang, Noise-tolerant single photon sensitive three-dimensional imager, *Nat. Commun.* **11**, 1 (2020).
- [17] A. M. Weiner, Femtosecond pulse shaping using spatial light modulators, *Rev. Sci. Instrum.* **71**, 1929 (2000).
- [18] A. Torralba and A. A. Efros, in *IEEE Conference on Computer Vision and Pattern Recognition (CVPR)* (2011) pp. 1521–1528.
- [19] K. Weiss, T. M. Khoshgoftaar, and D. Wang, A survey of transfer learning, *J. Big Data* **3**, 1 (2016).
- [20] K. Tang, Y. Da Wang, J. McClure, C. Chen, P. Mostaghimi, and R. T. Armstrong, Generalizable framework of unpaired domain transfer and deep learning for the processing of real-time synchrotron-based X-ray microcomputed tomography images of complex structures, *Phys. Rev. Appl.* **17**, 034048 (2022).
- [21] Y. Ganin, E. Ustinova, H. Ajakan, P. Germain, H. Larochelle, F. Laviolette, M. Marchand, and V. Lempitsky, Domain-adversarial training of neural networks, *J. Mach. Learn. Res.* **17**, 2096 (2016).
- [22] C. Szegedy, V. Vanhoucke, S. Ioffe, J. Shlens, and Z. Wojna, in *IEEE Conference on Computer Vision and Pattern Recognition (CVPR)* (2016) pp. 2818–2826.
- [23] R. Christoph and F. A. Pinz, in *Advances in Neural Information Processing Systems (NeurIPS)* (2016) pp. 3468–3476.
- [24] G. Yao, Y. Chen, Y. Liu, X. Hu, and Y. Pan, Robust photon-efficient imaging using a pixel-wise residual shrinkage network, arXiv:2201.01453 (2022).
- [25] P. K. Nathan Silberman, Derek Hoiem and R. Fergus, Indoor segmentation and support inference from rgbd images, in *European Conference on Computer Vision (ECCV)* (2012) pp. 746–760.
- [26] D. Scharstein and C. Pal, in *IEEE Conference on Computer Vision and Pattern Recognition (CVPR)* (2007) pp. 1–8.